remote sensing

MDPI

Article

Pulsed Orthogonal Time Frequency Space: A Fast Acquisition and High-Precision Measurement Signal for Low Earth Orbit Position, Navigation, and Timing

Dong Fu [1,2], Honglei Lin [1,2,*], Ming Ma [1,2], Muzi Yuan [1,2] and Gang Ou [1,2]

[1] College of Electronic Science and Technology, National University of Defense Technology, Changsha 410073, China; fudong@nudt.edu.cn (D.F.); maming@nudt.edu.cn (M.M.); ymz@nudt.edu.cn (M.Y.); ougang@nudt.edu.cn (G.O.)
[2] Key Laboratory of Satellite Navigation Technology, National University of Defense Technology, Changsha 410073, China
* Correspondence: linhonglei@nudt.edu.cn

Abstract: The recent rapid development of low Earth orbit (LEO) constellation-based navigation techniques has enhanced the ability of position, navigation, and timing (PNT) services in deep attenuation and interference environments. However, existing navigation modulations face the challenges of high acquisition complexity and do not improve measurement precision at the same signal strength. We propose a pulsed orthogonal time frequency space (Pulse-OTFS) signal, which naturally converts continuous signals into pulses through a special delay-Doppler domain pseudorandom noise (PRN) code sequence arrangement. The performance evaluation indicates that the proposed signal reduces at least 89.4% of the acquisition complexity. The delay measurement accuracy is about 8 dB better than that of the traditional binary phase shift keying (BPSK) signals with the same bandwidth. It also provides superior compatibility and anti-multipath performance. The advantages of fast acquisition and high-precision measurement are verified by processing the real signal in the developed software receiver. As Pulse-OTFS occupies only one time slot of a signal period, it can be easily integrated with OTFS-modulated communication signals and used as a navigation signal from broadband LEO satellites as an effective complement to the global navigation satellite system (GNSS).

Keywords: LEO PNT; satellite navigation; OTFS; pulsed signal; performance evaluation

Citation: Fu, D.; Lin, H.; Ma, M.; Yuan, M.; Ou, G. Pulsed Orthogonal Time Frequency Space: A Fast Acquisition and High-Precision Measurement Signal for Low Earth Orbit Position, Navigation, and Timing. *Remote Sens.* **2024**, *16*, 4432. https://doi.org/10.3390/rs16234432

Academic Editors: Ahmed El-Mowafy, Kan Wang and Xuhai Yang

Received: 29 September 2024
Revised: 25 November 2024
Accepted: 25 November 2024
Published: 27 November 2024

1. Introduction

The global navigation satellite system (GNSS) has become a fundamental component of the position, navigation, and timing (PNT) service, providing high-precision positioning and timing services. Meanwhile, the GNSS provides L-band microwave signals with high temporal resolution, extending its applications from positioning/navigation to remote sensing. However, the GNSS core constellations, such as the global positioning system (GPS) in medium Earth orbit (MEO), exhibit significant signal attenuation after long-distance propagation. This limits the applicability of the GNSS in environments with high levels of deep attenuation and interference, including dense urban areas and indoor settings, which presents a challenge for the further application of the GNSS [1]. In recent years, many proposals have been put forward regarding the construction of numerous large constellations of low Earth orbit (LEO) satellites, which accelerates the development of LEO constellations. It is anticipated that the integration of communication and navigation functions in LEO satellites will result in cost savings, as the construction of multiple systems will no longer be necessary [2]. The navigation system based on a LEO constellation offers several advantages, including strong signal strength, good dilution of precision (DOP) factor, fast geometric changes that help improve precise point positioning (PPP) performance, etc. [3–5].

Signal modulation is the key technology for satellite navigation systems and has a significant impact on the performance of navigation signals [6]. Some modulations have been employed in the GNSS, starting with binary phase shift keying (BPSK) [7]. To separate the spectrums of different signals on the same center frequency, binary offset carrier (BOC) modulation was adopted [8]. In the context of the modernization of the GNSS, two new modulation techniques were proposed, multiplexed BOC (MBOC) and alternate BOC (AltBOC) [9]. AltBOC is capable of providing a greater degree of flexibility in terms of the services it can offer than the former [10]. Nevertheless, the existing navigation modulation cannot be employed directly for LEO satellites for two primary reasons. On the one hand, the high Doppler caused by the LEO high-mobility channel significantly increases the acquisition complexity of traditional navigation modulation; despite chirp spread spectrum-like modulations effectively reducing the acquisition complexity, the measurement accuracy decreases [11,12]. On the other hand, the LEO constellation is primarily utilized for providing communication and Internet services [13,14]; existing navigation modulation techniques face challenges in meeting the requirements of broadband communication, despite their inherent data transmission capacity [15]. It is therefore evident that the implementation of navigation based on broadband communication modulation has become an important research area [16].

Orthogonal frequency division multiplexing (OFDM) modulation is widely adopted in communication systems, primarily due to its high spectral efficiency and strong anti-multipath performance. Furthermore, the Cramer-Rao lower bound (CRLB) for OFDM delay estimation is lower than that of BPSK [17], indicating that OFDM can improve the ranging accuracy of LEO satellite signals for future high-precision navigation applications. The navigation performance study of OFDM modulation showed that the code-tracking performance of OFDM was superior to that of the other GNSS signals with a pre-filtering bandwidth greater than 2 MHz [18]. Both the long-term evolution (LTE) and new radio (NR) systems successfully use the positioning reference signal (PRS) based on OFDM modulation for independent positioning [19–22]. As an OFDM-compatible modulation technique, orthogonal time frequency space (OTFS) has been considered a candidate for the next-generation communication system (6G) due to its excellent performance in high-mobility channels [23,24]. OTFS multiplexes information symbols over two-dimensional orthogonal basis functions in the delay-Doppler domain to combat the dynamics of the time-varying multipath channels [25]. As OTFS still converts symbols to the time-frequency domain, it can be expected to have a similar spectrum to OFDM, which means that OTFS improves communication performance under high-mobility channels while retaining the high-precision measurement capability of OFDM. Therefore, the application of OTFS modulation to the LEO satellite constellation is expected to provide better broadband communication and PNT services.

In recent years, OTFS has been investigated for use in LEO satellite constellations with the expectation of providing PNT services [26]. A recent study preliminarily explored the performance of OTFS as a LEO navigation signal; the results show that the theoretical delay and Doppler measurement accuracy of OTFS are better than BPSK, but no receiver was developed to verify the conclusions [27]. In another work, a red and blue frequency shift discriminator for OTFS modulation was designed to enable high-precision Doppler measurements with LEO signals [28]. An OTFS-based communication and navigation-integrated signal superimposes the AltBOC-modulated navigation message with quadrature amplitude-modulated communication data and then the symbols are transmitted via OTFS modulation, but the signal still utilizes time–domain PRN sequences for delay measurements rather than OTFS itself [29]. Some other studies have focused on pilot-based communication channel estimation [30–32], but these works cannot be directly applied to navigation.

Currently, LEO satellite navigation signals face a challenge, i.e., neither traditional navigation modulation nor OFDM reduces acquisition complexity; at least to the best of our knowledge, no studies have shown that they have an advantage in this regard. It is

well known that the acquisition of navigation signals is a three-dimensional search process of the satellite, the code phase, and the Doppler frequency. For a specific satellite, the acquisition complexity mainly depends on the loss introduced by the Doppler frequency offset in the signal cross-correlation, and the larger this loss, the longer the frequency search time required [7]. It can be anticipated that the Doppler loss for a pulsed signal is less than that for a continuous signal for the same power, because the former has a shorter coherent integration time, even though they have equal signal periods. The signal of the Locata system can be operated in a pulse amplitude modulation (PAM) with different duty cycles, power output, and pseudorandom noise (PRN) codes; PAM is commonly used to reduce interference and increase the working range, i.e., to overcome the "near-far" effect [33,34]. Numerous experiments have demonstrated that the Locata signals satisfy most scenarios where the GNSS is not available [35]. If the pulsed signals are applied to LEO satellites, it is expected that the correlation loss caused by Doppler frequency offset can be mitigated to reduce the acquisition complexity of the signal.

Inspired by OTFS modulation and pulsed signals, we propose Pulse-OTFS for LEO satellites that achieves low acquisition complexity and high-precision measurements, as well as better compatibility and anti-multipath performance. We make four contributions in this paper:

1. A novel signal named Pulse-OTFS is proposed in this paper, which has the advantages of both high-precision measurement and fast acquisition. We exploit the property of OTFS modulation to naturally convert a continuous signal into a pulsed signal by arranging multiple identical PRN code sequences in the delay-Doppler domain, which results in the generation of time–domain Pulse-OTFS signals with different duty cycles.
2. We introduce the mathematical model of the OTFS modulation and Pulse-OTFS signals and derive general expressions for the power spectral density (PSD) and autocorrelation function (ACF) of OTFS modulation, which are equally applicable to the proposed signal. We also discuss the relationship between the proposed signal properties and parameters as well as the connection with BPSK.
3. The navigation performance of Pulse-OTFS is evaluated in comprehensive detail and compared with that of the original OTFS signal, traditional GNSS signal, and Locata signal, i.e., Pulse-BPSK. The results indicate that the carrier power-to-noise density ratio (C/N_0 of the proposed signal is about 8 dB lower than that of the GNSS and Locata signals for the same code-tracking accuracy. This means that the proposed signal achieves higher measurement accuracy at the same C/N_0. Meanwhile, the acquisition complexity is reduced by at least 89.4%. It also has advantages in terms of compatibility and anti-multipath performance.
4. We implement an experimental platform based on software-defined radio (SDR) and verify the advantage in the fast acquisition and code-tracking accuracy of the proposed signal through a real analog channel. The experimental results are consistent with the theoretical performance analysis.

The remainder of this paper is organized as follows. Section 2 introduces the proposed Pulse-OTFS signal model and derives analytical expressions of the ACF and PSD. Section 3 evaluates the navigational performance of the proposed signal. Section 4 verifies the advantages of the proposed signal through an SDR-based experimental platform. Finally, the paper concludes in Section 5.

2. The Proposed Pulse-OTFS Signal

This section introduces the mathematical model of the OTFS modulation and the proposed signal, derives the expressions of ACF and PSD, and discusses the signal properties with different parameters.

2.1. Signal Model

The principle of OTFS modulation/demodulation is equivalent to adding an inverse symplectic fast Fourier transform (ISFFT) operation before OFDM modulation and a symplectic fast Fourier transform (SFFT) operation after OFDM demodulation, as shown in Figure 1. These two-dimensional transformations convert modulated symbols between the time-frequency domain and the delay-Doppler domain. The main signal parameters include the delay bins M, Doppler bins N, and bandwidth B, which are equal to the subcarrier number, symbols number, and bandwidth of OFDM, respectively.

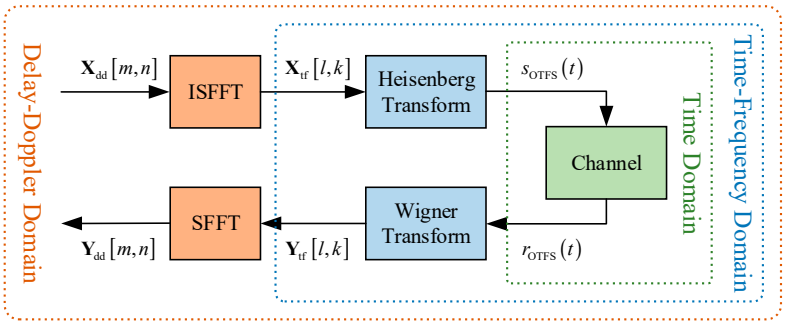

Figure 1. Block diagram of OTFS modulation.

The delay-Doppler transmitted symbol $\mathbf{X}_{\mathrm{dd}}[m,n]$ ($m = 0, \cdots, M-1, n = 0, \cdots, N-1$), is transformed to the time–frequency symbol by ISFFT:

$$\mathbf{X}_{\mathrm{tf}}[k,l] = \frac{1}{\sqrt{NM}} \sum_{n=0}^{N-1} \sum_{m=0}^{M-1} \mathbf{X}_{\mathrm{dd}}[m,n] e^{j2\pi\left(\frac{nl}{N} - \frac{mk}{M}\right)} \tag{1}$$

where $k = 0, \cdots, M-1, l = 0, \cdots, N-1$. Conversely, the time–frequency transmitted symbol $\mathbf{X}_{\mathrm{tf}}$ is transformed to the delay-Doppler symbol by SFFT:

$$\mathbf{X}_{\mathrm{dd}}[m,n] = \frac{1}{\sqrt{NM}} \sum_{l=0}^{N-1} \sum_{k=0}^{M-1} \mathbf{X}_{\mathrm{tf}}[k,l] e^{-j2\pi\left(\frac{nl}{N} - \frac{mk}{M}\right)} \tag{2}$$

The received symbols $\mathbf{Y}_{\mathrm{dd}}[m,n]$ and $\mathbf{Y}_{\mathrm{tf}}[k,l]$ can also be converted between the delay-Doppler domain and time–frequency domain using the above equations.

The time–domain baseband signal can be expressed as:

$$s(t) = \frac{1}{\sqrt{M}} \sum_{l=0}^{N-1} \sum_{k=0}^{M-1} \mathbf{X}_{\mathrm{tf}}[k,l] \Pi(t - lT) e^{j2\pi f_k (t - lT)} \tag{3}$$

where $\mathbf{X}_{\mathrm{tf}}$ is defined in (1), T denotes the symbol period, f_k is the frequency of the k-th subcarrier, and $f_k = k\Delta f$, Δf is the subcarrier spacing and $\Delta f = 1/T$, and $\Pi(t)$ is a rectangular pulse defined as:

$$\Pi(t) = \begin{cases} 1 & 0 \le t \le T \\ 0 & \text{otherwise} \end{cases} \tag{4}$$

2.1.1. Pulse-OTFS

Pulse-OTFS utilized as a navigation signal modulates the PRN code sequence spread spectrum navigation data on a two-dimensional delay-Doppler grid:

$$\mathbf{X}_{\mathrm{dd}}[m,n] = \mathrm{vec}_{M,N}^{-1}(d_k a_k) \tag{5}$$

where $k = 1, 2, \cdots, MN$, a_k is the PRN code sequence with a code length of MN, d_k is the navigation data, and usually remains constant for several signal frame periods, and $\mathrm{vec}_{M,N}^{-1}(\cdot)$ is the inverse vectorization operator.

The navigation data of the proposed Pulse-OTFS is spread by N identical PRN code sequences in a frame, that is, the code length of the PRN code sequence is M, and the navigation data are the same as (5). Its matrix form can be expressed as $\mathbf{X}_{\mathrm{dd}} = \mathbf{a}_{M\times 1} \otimes \mathbf{d}_{1\times N}$, where $\otimes$ is the Kronecker product. According to the matrix form of ISFFT [25], the equivalent time–frequency matrix is:

$$\begin{aligned} \mathbf{X}_{\mathrm{tf}} &= \mathbf{F}_M \mathbf{X}_{\mathrm{dd}} \mathbf{F}_N^{\dagger} \\ &= \mathbf{F}_M (\mathbf{a}_{M\times 1} \otimes \mathbf{d}_{1\times N}) \mathbf{F}_N^{\dagger} \\ &= (\mathbf{F}_M \mathbf{a}_{M\times 1}) \otimes (\mathbf{d}_{1\times N} \mathbf{F}_N^{\dagger}) \\ &= \left[\sqrt{N}\mathbf{A}_{M\times 1}, \mathbf{0}_{M\times(N-1)}\right] \end{aligned} \tag{6}$$

where $\mathbf{F}_M$ and $\mathbf{F}_N$ are the discrete Fourier transform matrices of dimensions $M \times M$ and $N \times N$, respectively, and $\mathbf{A}_{M\times 1}$ is the Fourier transform of the PRN code sequence.

Equation (6) illustrates that only the first column element in the time-frequency matrix $\mathbf{X}_{\mathrm{tf}}$ is non-zero, i.e., the time–domain baseband signal is only non-zero for the duration of the first symbol in a frame signal period, and the duty cycle is $1/N$. This is why we call it Pulse-OTFS.

Consider a Pulse-OTFS system with M delay bins and N Doppler bins. The signal has a total bandwidth of B and occupies a frame duration (signal period) of NT, and the number of transmitted PRN code chips is $M \times N$. Then, the following relationship can be established:

$$\begin{cases} f_c = MN/(NT) = M\Delta f = B \\ T_c = 1/f_c = 1/B = T/M \end{cases} \tag{7}$$

where f_c is the PRN code rate and T_c is the code chip duration.

Note that, unlike traditional GNSS signals where the bandwidth of the main lobe is twice the PRN code rate, the main lobe bandwidth of OTFS/Pulse-OTFS is equal to the PRN code rate, which has a significant impact on its PSD and ACF properties; we will analyze this later in this section.

In this paper, the OTFS and Pulse-OTFS signals are simply denoted by OTFS(α, β) and Pulse-OTFS(α, β), where

$$\begin{cases} \alpha = f_c/f_0 \\ \beta = f_c/\Delta f \end{cases} \tag{8}$$

where f_0 = 1.023 MHz is the reference frequency commonly used in the GNSS signal, α, β are positive integers, and β is equal to the delay bins/subcarrier numbers M.

2.1.2. Transmission and Reception Process

Based on the previous introduction, we can summarize the transmission and reception process of Pulse-OTFS signals for LEO PNT as follows:

Step 1: The navigation data are spread by the PRN code sequences and are arranged in the delay-Doppler grid by (5).

Step 2: The delay-Doppler matrix is converted to a time–frequency domain signal by ISSFT via (1). The transformed time–frequency matrix is expressed as (6).

Step 3: The time–frequency matrix is converted to a time–domain continuous baseband signal by the OFDM modulator via (3).

Step 4: The time-domain continuous baseband signal is modulated to RF by the carrier and transmitted over the antenna.

Now, we have completed the transmission process of the signal. The transmitted signal travels across the LEO channel and is received by the following steps:

Step 1: The RF signal received by the antenna is down-converted to a time–domain baseband signal, and the continuous signal is converted to a discrete signal by an analog-to-digital converter (ADC).

Step 2: The receiver uses the locally stored replica of the time domain signal to acquire the received signal to estimate the code phase and Doppler frequency.

Step 3: The acquired signal is sent into the tracking loop to perform fine delay and Doppler measurements and obtain the demodulated navigation data.

Step 4: The receiver uses the measurements and navigation data output from the tracking loop to complete the positioning and timing process.

It can be seen that when Pulse-OTFS signals are employed for navigation, the reception process is the same as that of traditional navigation signals. This process is different from the communication signal in Figure 1. Since the orthogonality of the PRN code is not changed either in the time domain or the delay-Doppler domain, the delay measurement of Pulse-OTFS can also be completed in the time domain.

2.2. Derivation of ACF and PSD

2.2.1. Derivation of ACF

The ACF of OTFS can be written as:

$$\begin{aligned} &R(t+\tau,t) = E\left(\overline{s(t)}s(t+\tau)\right) \\ &= \frac{1}{M}E\left(\sum_{l=-\infty}^{\infty}\sum_{k=0}^{M-1}\overline{\mathbf{X}_{\mathrm{tf}}[k,l]\Pi(t-lT)e^{j2\pi k\Delta f(t-lT)}}\sum_{n=-\infty}^{\infty}\sum_{m=0}^{M-1}\mathbf{X}_{\mathrm{tf}}[m,n]\Pi(t+\tau-nT)e^{j2\pi m\Delta f(t+\tau-nT)}\right) \\ &= \frac{1}{M}\sum_{i=-\infty}^{\infty}\sum_{r=-\infty}^{\infty}R_{\mathbf{X}_{\mathrm{tf}}}(i,r)\sum_{l=-\infty}^{\infty}\sum_{k=0}^{M-1}\overline{\Pi(t-lT)e^{j2\pi k\Delta f(t-lT)}}\cdot\Pi(t+\tau-(l+r)T)e^{j2\pi(k+i)\Delta f(t+\tau-(l+r)T)} \end{aligned} \tag{9}$$

Since ISFFT does not change the power and orthogonality of information symbols [25], then the power of information symbols is:

$$E\left[\overline{\mathbf{X}_{\mathrm{tf}}}\mathbf{X}_{\mathrm{tf}}\right] = E\left[\overline{\mathbf{X}_{\mathrm{dd}}}\mathbf{X}_{\mathrm{dd}}\right] = \sigma_{\mathrm{X}}^2 \tag{10}$$

where $\overline{\mathbf{X}}$ is the conjugation of $\mathbf{X}$. $\sigma_{\mathrm{X}}^2 = 1$ when the information symbols are PRN code chips. The autocorrelation of the information symbol is

$$R_{\mathbf{X}_{\mathrm{tf}}}(i,r) = \begin{cases} 1 & i=0 \ \&\ r=0 \\ 0 & \text{otherwise} \end{cases} \tag{11}$$

We can observe from (9) that the ACF $R(t+\tau,t)$ is a function with a period of T for variable t, and $s(t)$ conforms to the definition of generalized cyclostationary processes. Thus, the variable t in $R(t+\tau,t)$ can be eliminated, and the ACF $R(\tau)$ can be written as:

$$\begin{aligned} R(\tau) &= \frac{1}{T}\int_0^T R(t+\tau,t)\mathrm{d}t \\ &= \frac{1}{MT}\int_0^T\sum_{i=-\infty}^{\infty}\sum_{r=-\infty}^{\infty}R_{\mathbf{X}_{\mathrm{tf}}}(i,r)\sum_{l=-\infty}^{\infty}\sum_{k=0}^{M-1}\overline{\Pi(t-lT)e^{j2\pi k\Delta f(t-lT)}}\cdot\Pi(t+\tau-(l+r)T)e^{j2\pi(k+i)\Delta f(t+\tau-(l+r)T)}\mathrm{d}t \\ &= \frac{1}{MT}\sum_{i=-\infty}^{\infty}\sum_{r=-\infty}^{\infty}R_{\mathbf{X}_{\mathrm{tf}}}(i,r)\sum_{l=-\infty}^{\infty}\int_{-lT}^{(1-l)T}\sum_{k=0}^{M-1}\overline{\Pi(t)e^{j2\pi k\Delta ft}}\cdot\Pi(t+\tau-rT)e^{j2\pi(k+i)\Delta f(t+\tau-rT)}\mathrm{d}t \\ &= \frac{1}{MT}\sum_{i=-\infty}^{\infty}\sum_{r=-\infty}^{\infty}R_{\mathbf{X}_{\mathrm{tf}}}(i,r)\sum_{k=0}^{M-1}e^{j2\pi k\Delta f(\tau-rT)}\cdot\int_{-\infty}^{\infty}\overline{\Pi(t)}\Pi(t+\tau-rT)e^{j2\pi i\Delta f(t+\tau-rT)}\mathrm{d}t \end{aligned} \tag{12}$$

Substituting (11) into (12) yields:

$$\begin{aligned} R(\tau) &= \frac{1}{M}\sum_{k=0}^{M-1}e^{j2\pi k\Delta f\tau}\frac{1}{T}\int_{-\infty}^{\infty}\overline{\Pi(t)}\Pi(t+\tau)\mathrm{d}t \\ &= \frac{1}{M}\sum_{k=0}^{M-1}e^{j2\pi k\Delta f\tau}\left(1-\frac{|\tau|}{T}\right) \end{aligned} \tag{13}$$

The above equation is both the theoretical expression for the ACF of OTFS and Pulse-OTFS signals since the Pulse-OTFS signal is non-zero for at least one complete symbol duration.

2.2.2. Derivation of PSD

Similar to OFDM, the information symbols on each subcarrier or symbol period of the signal in (3) are statistically independent and orthogonal stochastic processes [36,37]. Consequently, the PSD of the Pulse-OTFS modulation is:

$$G(f) = \frac{T}{M}\sum_{k=0}^{M-1}\left|\frac{\sin[\pi(f-f_k)T]}{\pi(f-f_k)T}\right|^2 \tag{14}$$

To verify the correctness of (14), we compared the theoretical and simulation PSDs of the Pulse-OTFS(1,1023) signal, where f_c is 1.023 Mcps, the sampling rate is 2 MHz, the delay bins M = 1023, the Doppler bins N = 10, and the signal duration is 100 ms. Figure 2 shows that the theoretical PSD is consistent with the simulation result.

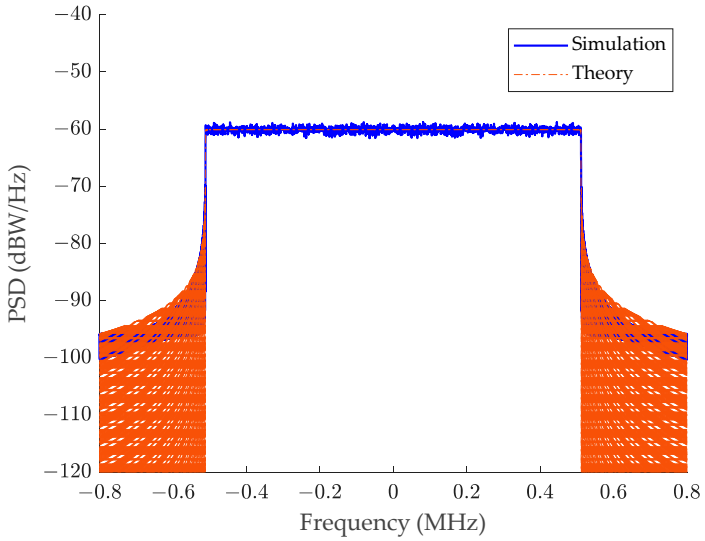

Figure 2. PSDs of the Pulse-OTFS signal.

2.2.3. Analysis of PSD and ACF

Since the properties of PSD and ACF strongly affect the navigation performance of the signal, we discuss the PSD and ACF with different parameters in this section. To understand the difference between the proposed signal and the traditional GNSS and Locata signals, we have included BPSK(5) and Pulse-BPSK(5) signals with a 10 MHz bandwidth. The delay bins M and the signal bandwidth B are the main parameters affecting the PSD and ACF of Pulse-OTFS, so we give the PSD and ACF results of Pulse-OTFS with signal bandwidths of 1 MHz and 10 MHz and delay bins of 1, 64, and 1023 in Figures 3 and 4, respectively.

Figure 3 illustrates that the PSD main lobe of the Pulse-OTFS signal is flat and its out-of-band (OOB) emission decreases as the delay bin increases. Interestingly, the PSD degrades to that of a BPSK modulation with twice the bandwidth of Pulse-OTFS when the delay bin is equal to 1. Compared to BPSK and Pulse-BPSK, the signal energy of Pulse-OTFS is concentrated within the main lobe, and its OOB emission is much lower, which is an advantage in some bands where the spectrum is strictly guarded.

As can be seen from Figure 4, for Pulse-OTFS signals with different parameters, the main peak of the ACF is steeper the wider the signal bandwidth is, while there is not much difference between the ACFs with different delay bins, except that its ACF when the delay bin is equal to 1 degrades to that of the BPSK modulation with twice the bandwidth, which is similar to the results in Figure 3. The main peak of the ACF of Pulse-OTFS in Figure 4 is

steeper than that of BPSK and Pulse-BPSK for the equal bandwidth, which enables more precise determination of the time of arrival, resulting in enhanced delay resolution and measurement accuracy. This precision is particularly crucial for applications demanding exact positioning or synchronization. But one may ask the question, although the ACF of the Pulse-OTFS signal has a steep main peak, it has a lot of sidelobes; could this lead to false locking during tracking similar to the BOC signal? The answer is no because its S-curve has only one zero-crossing point; it can be found in the next section.

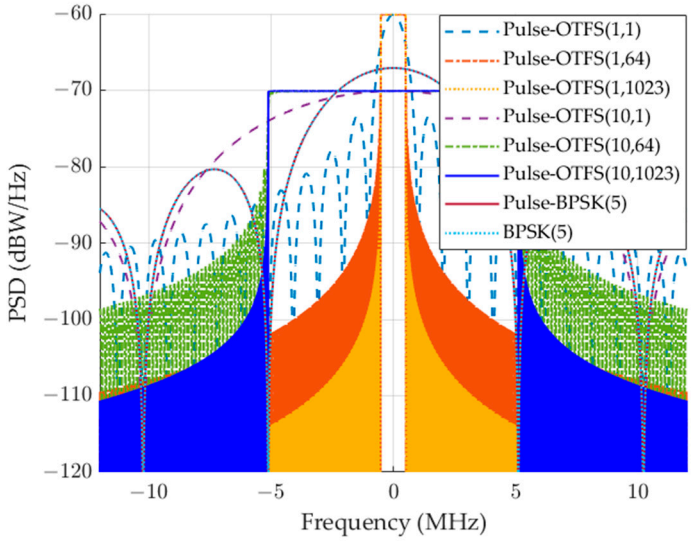

Figure 3. Comparison of PSDs for Pulse-OTFS signals with BPSK(5), and Pulse-BPSK(5).

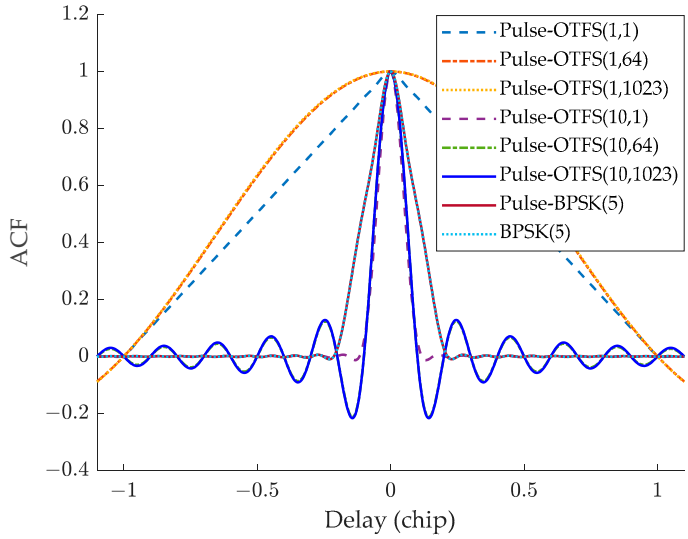

Figure 4. Comparison of ACFs for Pulse-OTFS signals with BPSK(5), and Pulse-BPSK(5).

3. Performance Evaluation

In this section, we evaluate the navigation performance of the proposed signal and compare it with the original OTFS, traditional GNSS, and Locata signals. The selected traditional navigation signal is BPSK(5), the selected Locata signal is Pulse-BPSK(5), and the duty cycle of the pulsed signals is 1/10.

3.1. Quantization Loss

Most RF transmitters and receivers in modern communication or navigation systems use digital-to-analog converters (DACs) and ADCs to implement the transmission of

continuous-time signals and the reception of discrete-time signals. Due to limited resolution, ADCs tend to introduce quantization errors into the system, which causes a loss in system performance. Unlike BPSK, the amplitude of the OTFS time–domain signal does not have a constant envelope, and a higher bit resolution may be required for amplitude quantization; therefore, the quantization loss of the proposed signal is analyzed in this section. To simplify the problem, we assume that the signal is quantized before it is transmitted. Therefore, the quantization loss is for the entire system. The receiver does not suffer additional quantization loss.

When the signal is Q-bit quantized ($Q \geq 1$), there are $2^Q - 1$ quantization levels and 2^Q quantization results, and the quantization function can be expressed as:

$$\mathbb{Q}[n] = \begin{cases} -2^Q + 1, & s[n] \leq \left(2^{Q-1} - 1\right)L \\ 2i + 1, & iL < s[n] \leq (i+1)L \\ 2^Q - 1, & s[n] > \left(2^{Q-1} - 1\right)L \end{cases} \tag{15}$$

where $i \in \left\{-2^{Q-1} + 1, -2^{Q-1} + 2, \ldots, 2^{Q-1} - 2,\right\}$. L is the quantization interval, and the value of L is related to the quantization threshold and the number of quantization levels. If the quantization threshold H is determined, we have

$$L = \frac{H}{2^{Q-1}} \tag{16}$$

In general, the quantization threshold is set to a constant value.

According to the Wiener–Khintchine theorem, it is known that the ACF of a signal is the inverse Fourier transform of its corresponding PSD. Therefore, the PSD of the quantized signal also reflects the quantization loss of the ACF. The closer the power ratio of the main lobe of the quantized PSD is to that before quantization, the less the loss of the ACF. The simulation results of the PSD of OTFS(10,1023) with different quantization bits are given in Figure 5. The main lobe bandwidth of the signal is 10.23 MHz, the sampling rate is 20 MHz, and $+\infty$ represents no quantization. We can observe from the figure that the sidelobe of the OTFS rises as the quantized bits of the signal decrease, which makes the power ratio of the main lobe decrease and then the loss of the ACF becomes greater.

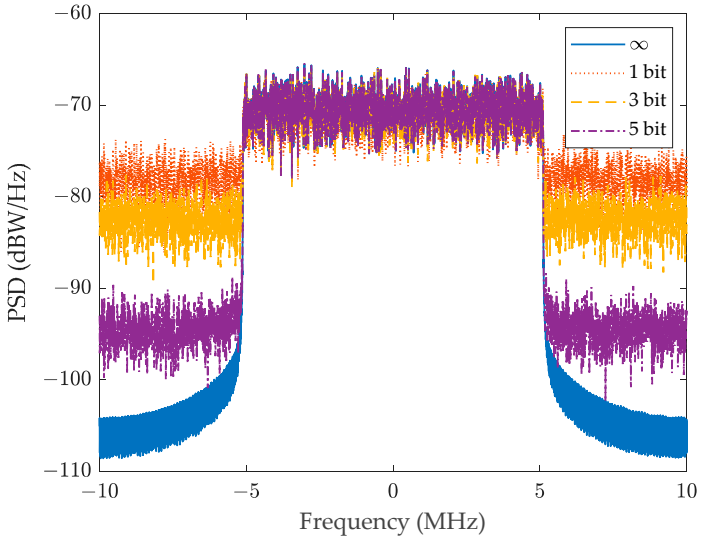

Figure 5. Simulation PSDs with different quantization bits for OTFS(10,1023).

Table 1 gives the corresponding quantization losses for OTFS(10,1023) with different quantization bits Q. We can also calculate the main lobe power ratio of BPSK(5) as 92.45% in all cases, which is because the amplitude of BPSK has a constant envelope. Comparing the results in Table 1, we can see that the main lobe power ratio of OTFS is lower than that of BPSK when the quantization bits $Q \leq 2$. At this moment, the utilization of the transmitter power is not as efficient as that of BPSK; the quantization loss is around -0.75 dB. The main lobe power ratio of OTFS is higher than that of BPSK and its quantization loss is significantly reduced if $Q \geq 3$. Therefore, 3 bits can be selected to exploit the performance of OTFS when hardware resources are sufficient.

Table 1. Power ratio of the main lobe and corresponding quantization loss for the OTFS signal.

Q (bit)	1	2	3	4	5	$+\infty$
Power ratio of the main lobe (%)	83.86	84.24	94.03	98.52	99.59	99.93
Quantization loss (dB)	-0.76	-0.74	-0.26	-0.06	-0.01	0

3.2. Acquisition Performance

3.2.1. Ambiguity Function

The ambiguity function is an important method to analyze the acquisition performance of navigation signals. If the channel delay and Doppler are τ and f_d, respectively, and the coherent integration time is T_{coh}, the ambiguity function can be written as:

$$A(\tau, f_d) = \int_0^{T_{coh}} s(t)\overline{s(t-\tau)}e^{j2\pi f_d t}\mathrm{d}t \tag{17}$$

Substituting (3) into (17) yields

$$\begin{aligned} A(\tau, f_d) &= \frac{1}{M}\int_0^{T_{coh}}\sum_{k=0}^{M-1}\mathbf{X}_{\mathrm{tf}}[k]\Pi(t)e^{j2\pi k\Delta f t}\cdot\overline{\mathbf{X}_{\mathrm{tf}}[k]\Pi(t-\tau)e^{j2\pi k\Delta f(t-\tau)}}e^{j2\pi f_d t}\mathrm{d}t \\ &= \frac{1}{M}\sum_{k=0}^{M-1}e^{j2\pi k\Delta f\tau}\int_0^{T_{coh}}\Pi(t)\overline{\Pi(t-\tau)}e^{j2\pi f_d t}\mathrm{d}t \\ &= \frac{1}{M}\sum_{k=0}^{M-1}e^{j2\pi k\Delta f\tau}\left(\frac{\sin\pi f_d(T_{coh}-|\tau|)}{\pi f_d(T_{coh}-|\tau|)}\right)\left(1-\frac{|\tau|}{T}\right) \end{aligned} \tag{18}$$

The ambiguity function envelope of OTFS is

$$|A(\tau, f_d)| = \left|\frac{1}{M}\sum_{k=0}^{M-1}e^{j2\pi k\Delta f\tau}\left(\frac{\sin\pi f_d(T_{coh}-|\tau|)}{\pi f_d(T_{coh}-|\tau|)}\right)\left(1-\frac{|\tau|}{T}\right)\right| \tag{19}$$

Figure 6 shows the ambiguity function envelope of Pulse-OTFS(10,1023) with a signal period of 1 ms and Doppler bins of 10. The variation in the ambiguity function envelope along the delay axis is consistent with the absolute value of the ACF, while the variation in the correlation values along the Doppler axis is similar to the GNSS signal. However, we can see from the figure that the correlation loss of the proposed signal along the Doppler axis is much less, its 3 dB loss of the peak corresponds to a frequency offset range up to [-4.43 kHz, 4.43 kHz]. This is because the coherent integration time T_{coh} is equal to the signal period NT, but the effective coherent integration time $T_{eff} = T$ as the Pulse-OTFS signal is not zero for only the first symbol duration T.

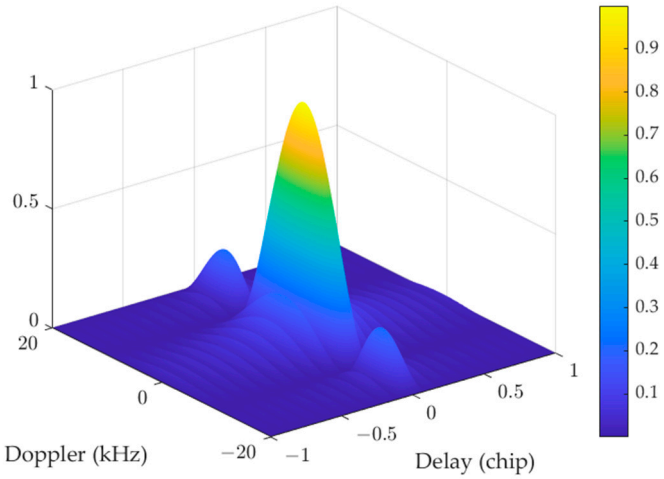

Figure 6. Ambiguity function envelope of Pulse-OTFS(10,1023).

3.2.2. Acquisition Complexity

The signal-to-noise ratio (*SNR*) of the Pulse-OTFS receiver output is

$$SNR = \frac{I^2 + Q^2}{N_0/T_{coh}} = \frac{PT_{coh}}{N_0}\left(\frac{1}{M}\sum_{k=0}^{M-1} e^{j2\pi k\Delta f\tau}\right)^2\left(\frac{\sin\pi f_d(T_{coh}-|\tau|)}{\pi f_d(T_{coh}-|\tau|)}\right)^2\left(1-\frac{|\tau|}{T}\right)^2 \quad (20)$$

In the case of a desired signal being in existence, the correlation value will satisfy the Rice distribution. Conversely, in the case of no desired signal being in existence, the correlation value will satisfy the Rayleigh distribution. The acquisition threshold and acquisition probability are as follows

$$\begin{cases} V_t = \sigma_n\sqrt{-2\ln P_{fa}} \\ P_d = \int_{V_t}^{\infty} f(v)\mathrm{d}v \end{cases} \quad (21)$$

where $\sigma_n^2 = N_0/T_{coh}$ is the noise power, P_{fa} is the false alarm probability, and $f(v)$ is the Rice distribution probability density function (PDF).

Doppler tolerance is referred to as the offset of the Doppler frequency when the signal processing gain is at its minimum allowable level. This directly affects the division of frequency grids in two-dimensional search, as well as the average acquisition time. The Doppler tolerance is defined by the following equation

$$SNR_{Th} = func(\tau, f_{d,\max}) \quad (22)$$

where SNR_{Th} is the output *SNR* threshold during the acquisition process and $f_{d,\max}$ is the maximum Doppler offset that satisfies the minimum output *SNR* threshold.

If the maximum Doppler offset $f_{d,\max}$ satisfies the false alarm probability P_{fa} and acquisition threshold V_t, generally, $2f_{d,\max}$ is selected as the Doppler search interval to calculate the number of Doppler frequency searches. Substituting the *SNR* threshold $SNR_{Th} = -2\ln P_{fa}$ and $f_{d,\max}$ into (20) yields

$$\left|\frac{1}{M}\sum_{k=0}^{M-1} e^{j2\pi k\Delta f\tau}\left(\frac{\sin\pi f_d(T_{coh}-|\tau|)}{\pi f_d(T_{coh}-|\tau|)}\right)\left(1-\frac{|\tau|}{T}\right)\right| = \sqrt{\frac{N_0}{PT_{coh}}SNR_{Th}} \quad (23)$$

The left part of (23) is the exact ambiguity function envelope; then, we have the peak envelope of the ambiguity function for different Doppler offset:

$$\begin{aligned} A(f_d) &= \max_{\tau}\left(\left|\frac{1}{M}\sum_{k=0}^{M-1} e^{j2\pi k\Delta f\tau}\left(\frac{\sin\pi f_d(T_{coh}-|\tau|)}{\pi f_d(T_{coh}-|\tau|)}\right)\left(1-\frac{|\tau|}{T}\right)\right|\right) \\ &= \left|\frac{1}{M}\sum_{k=0}^{M-1}\mathrm{sinc}(f_d T_{coh})\right| \end{aligned} \tag{24}$$

The Doppler search range of the LEO satellite at 1500 km altitude is (−40 kHz, +40 kHz) with a 2 GHz carrier frequency [38]. Using a parallel code phase search (PCS) scheme and signal period of 1 ms, the threshold on the right side of (23) is 0.64, then the corresponding search interval of both BPSK and OTFS is 500 Hz, and the number of serial searches for Doppler frequency is 161. However, the Doppler search interval of Pulse-OTFS and Pulse-BPSK are both 500 N Hz and the number of serial searches for Doppler frequency is $160/N + 1$, where the duty cycles are both $1/N$ for Pulse-OTFS and Pulse-BPSK. Assuming that the same sampling rate and bit resolution are used for all signals to simplify the analysis of acquisition complexity, the same number of multiplications and additions are required to perform a PCS, denoted Δ_m and Δ_a, respectively. Thus, the overall acquisition complexity depends on the number of complex multiplications and additions.

The acquisition complexity of different signals is listed in Table 2. Figure 7 shows the multiplication and addition complexity ratio of Pulse-OTFS/Pulse-BPSK to OTFS/BPSK as a function of Doppler bins N. The results illustrate that the acquisition complexity of pulsed signals is significantly lower than that of continuous signals, but the decrease in complexity is not linear with N because the Doppler search range is fixed, and the number of Doppler frequency searches tends to be constant when N is large. Commonly, $1/N$ is not greater than 0.1; then, substituting $N = 10$ into Table 2 yields the number of multiplications and additions of the pulsed signals. In this case, the number of multiplications and additions for Pulse-OTFS and Pulse-BPSK signal acquisition is reduced by at least 89.4% compared to OTFS and BPSK signals.

Table 2. Acquisition complexity for different signals.

Signals	Pulse-OTFS	Pulse-BPSK	OTFS	BPSK
Multiplication	$(160/N+1)\Delta_m$	$(160/N+1)\Delta_m$	$161\Delta_m$	$161\Delta_m$
Addition	$(160/N+1)\Delta_a$	$(160/N+1)\Delta_a$	$161\Delta_a$	$161\Delta_a$

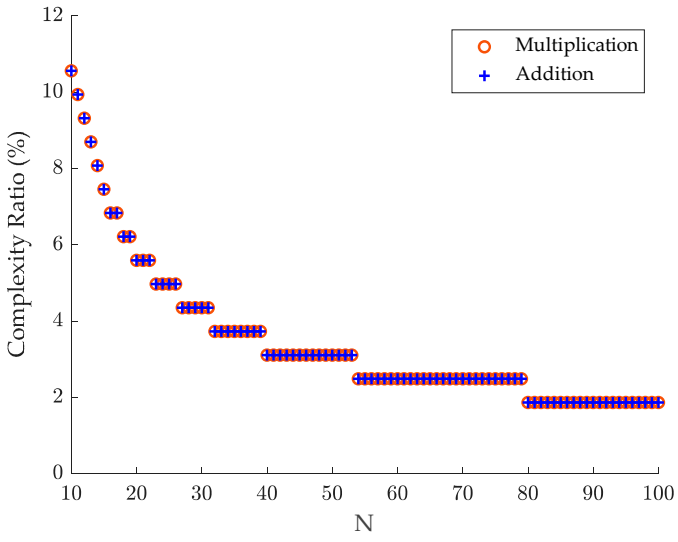

Figure 7. Multiplication and addition complexity ratio of Pulse-OTFS/Pulse-BPSK to OTFS/BPSK.

3.2.3. Acquisition Probability

We next analyze the acquisition probability. From (20), it is easy to observe that the *SNR* of all signals at the output of the correlator is the same if the delay offset τ and Doppler offset f_d are zero and the received signal power and coherent integration time are equal, where coherent integration time is an integer multiple of the signal period. However, with the same total false alarm probability, the higher the number of Doppler frequency searches, the smaller the false alarm probability per search, and the lower the corresponding detection probability.

The acquisition of navigation signals is essentially a detection problem, the Doppler estimation accuracy depends mainly on the frequency search step. The correlation loss introduced by the frequency offset is at its maximum when the true Doppler frequency falls exactly at 1/2 of the two search frequency points, and the acquisition probability is the worst. In the following, we analyze the acquisition performance of the proposed signals under different Doppler frequencies and significant Doppler shift scenarios. We set the signal bandwidth to 10.23 MHz, the sampling frequency to 20.46 MHz, and the total false alarm probability to 10^{-3}, $N = 10$, $T_{coh} = 1$ ms. The theoretical detection probabilities of different signals can be obtained as shown in Figure 8. Where 0 Hz and 40 kHz in parentheses are the minimum and maximum channel Doppler, respectively. In addition, 37.25 kHz and 37.5 kHz in parentheses are the middle frequencies between two adjacent frequency search points for continuous and pulsed signals, respectively.

Analyzing the results shown in Figure 8, we can conclude the following. Firstly all of the signals have the same and highest acquisition probability at 0 Hz and 40 kHz; this is because despite 40 kHz being a significant Doppler shift, it falls exactly at the frequency search points at which it does not introduce correlation loss. Secondly, the acquisition probabilities of the Pulse-OTFS and Pulse-BPSK signals at 37.5 kHz and OTFS and BPSK at 37.25 kHz are about 0.9 dB lower than that at 0 Hz and 40 kHz, respectively, which represents the worst detection probability. Finally, Pulse-OTFS and Pulse-BPSK have about 1 dB better detection performance than OTFS and BPSK at the same Doppler frequency offset and carrier power-to-noise density ratio C/N_0. The proposed signal improves the acquisition probability compared to the continuous signals with the same total false alarm probability and C/N_0.

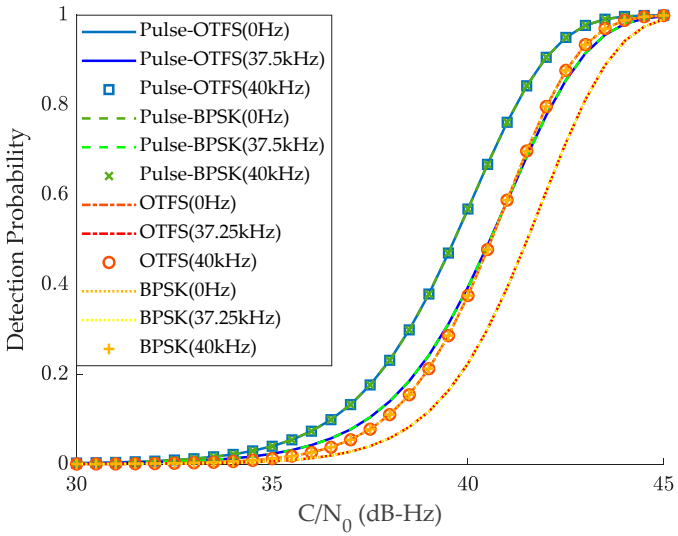

Figure 8. Detection probability of different signals.

3.3. Code-Tracking Performance

In the case that the front-end filter is assumed to be ideal, the CRLB of the code-tracking error can be approximated [39]:

$$\tau_{\mathrm{CRLB}} = \frac{B_L(1 - 0.5B_L T_{coh})}{(2\pi)^2 \frac{C}{N_0} \int_{-B_r/2}^{B_r/2} f^2 G_n(f) \mathrm{d}f} \tag{25}$$

where $B_L$is the equivalent noise bandwidth of the code-tracking loops, C/N_0 is the carrier power-to-noise density ratio, B_r is the pre-filtering bandwidth, and $G_n(f)$ is the normalized PSD of the signal.

Let us further suppose that the parameters of the code-tracking loops are fixed. In such a scenario, the code-tracking performance for different modulations is dependent on the integral term in (25), which is defined as the Gabor bandwidth:

$$\Delta f_{\mathrm{Gabor}} = \sqrt{\int_{-B_r/2}^{B_r/2} f^2 G_n(f) \mathrm{d}f} \tag{26}$$

The greater the Gabor bandwidth, the better the code-tracking performance will be. Furthermore, the variance in the code-tracking error with the thermal noise for a widely used non-coherent early–late processing (NELP) delay-locked loop (DLL) is [40]

$$\sigma^2_{\mathrm{NELP}} = \frac{B_L(1 - 0.5B_L T_{coh}) \int_{-B_r/2}^{B_r/2} G_n(f) \sin(\pi f d)^2 \mathrm{d}f}{(2\pi)^2 \frac{C}{N_0} \left(\int_{-B_r/2}^{B_r/2} f G_n(f) \sin(\pi f d) \mathrm{d}f \right)^2} \cdot \left(1 + \frac{\int_{-B_r/2}^{B_r/2} G_n(f) \cos(\pi f d)^2 \mathrm{d}f}{T_{coh} \frac{C}{N_0} \left(\int_{-B_r/2}^{B_r/2} G_n(f) \cos(\pi f d) \mathrm{d}f \right)^2} \right) \tag{27}$$

where d is the early–late spacing of the correlator.

Figure 9 shows the Gabor bandwidth and the code-tracking accuracy of the NELP DLL for all of the signals we compared. The pre-filtering bandwidth is 20 MHz, $d = 1$ chip, and $B_L = 1$. To analyze the signal tracking performance under extreme conditions, Figure 9b includes the theoretical tracking accuracies for the coherent integration time T_{coh} of 1 ms and 10 ms, C/N_0 of 25 dB·Hz to 45 dB·Hz.

The results indicate that pulsed signals have the same code-tracking accuracy compared to continuous signals. The longer the coherent integration time, the higher the tracking accuracy at the same modulation and C/N_0. The code-tracking accuracy of OTFS(10,1023) and Pulse-OTFS(10,1023) is higher than that of BPSK(5) and Pulse-BPSK(5). This means that to achieve the same code-tracking accuracy, the C/N_0 of BPSK(5) and Pulse-BPSK(5) is about 8 dB higher than that of OTFS(10,1023) and Pulse-OTFS(10,1023). Obviously, the proposed signal has the advantage of code-tracking accuracy.

In a code-tracking loop, the discriminator curve (S-curve) is used to reflect the discriminator gain and the zero-crossing point of the received signal. Figure 10 shows the simulated S-curve of Pulse-OTFS(10,1023), Pulse-BPSK(5), OTFS(10,1023), and BPSK(5), where $T_{coh} = 1$ ms, $d = 1$ chip. Since a larger pre-filtering bandwidth does not necessarily give better performance in BPSK, we set the pre-filter bandwidth to 20 MHz to ensure a fair comparison. In contrast with BOC modulation, both OTFS(10,1023) and Pulse-OTFS(10,1023) have only one zero-crossing point within 1 chip delay offset and can therefore be received unambiguously. The discriminator gain is also higher than that of Pulse-BPSK(5) and BPSK(5), so the code-tracking performance of the proposed signal is superior to the latter.

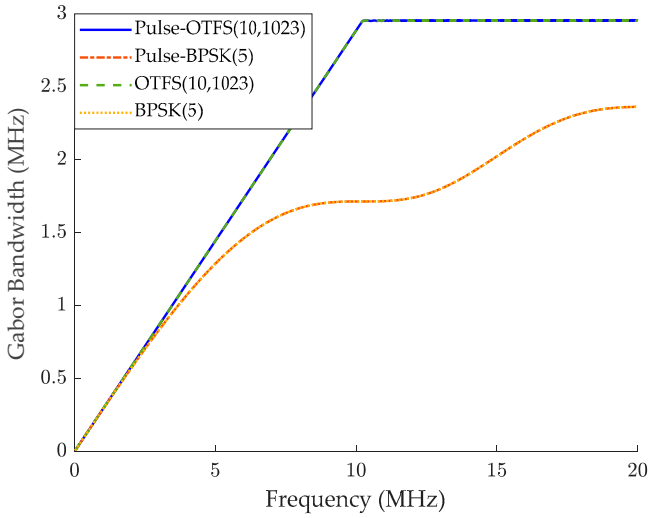

(**a**)

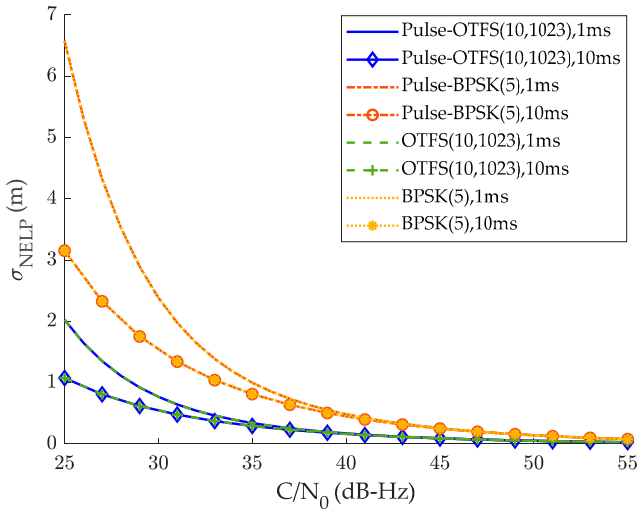

(**b**)

Figure 9. Comparison of code-tracking performance for different signals. (**a**) Gabor bandwidth and (**b**) NELP DLL code-tracking error with a 20 MHz pre-filtering bandwidth.

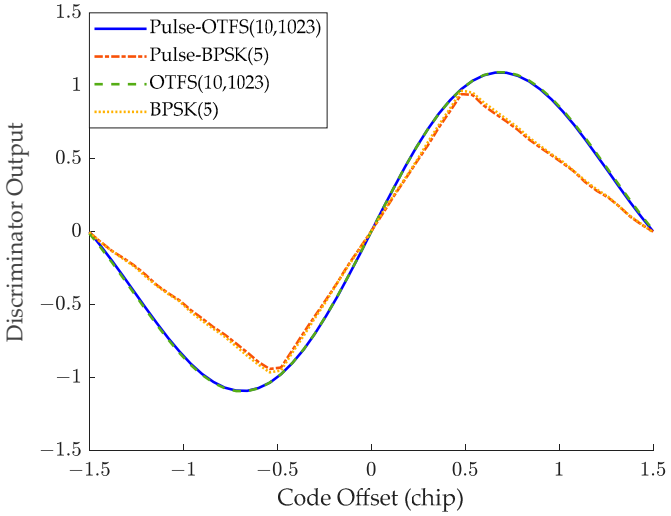

Figure 10. Comparison of S-curves for different signals with a 20 MHz pre-filtering bandwidth.

3.4. Anti-Multipath Performance

The anti-multipath performance of navigation signals is usually evaluated with the code-tracking multipath error envelope and the average multipath envelope error based on an NELP DLL [41,42]. The multipath error envelope is the maximum deviation caused by the multipath effect, which reflects the worst case of multipath error corresponding to a specific geometric delay. The average multipath envelope error is the accumulated average of the multipath error envelope with the geometric delay, which reflects the overall situation of the multipath deviation within a certain geometric delay.

The multipath error envelope is quantified as a function of the relative delay between two rays, with the approximate expression being

$$\varepsilon \approx \frac{\pm a \int_{-B_r/2}^{B_r/2} G_n(f) \sin(2\pi f\tau) \sin(\pi f d) df}{2\pi \int_{-B_r/2}^{B_r/2} f G_n(f) \sin(\pi f d)[1 \pm a\cos(2\pi f\tau)] df} \tag{28}$$

where a is the multipath-to-direct ratio (MDR), generally below -6 dB, ε is the delay estimation error, and τ is the geometric path delay.

The average multipath error envelope is calculated by the cumulative sum of the absolute values of the multipath error envelope, whereby the values are added together to give a total. The relationship between the average multipath error envelope can be written as follows:

$$\varepsilon_a \approx \frac{1}{\tau}\int_0^{\tau} \left[\frac{\left|\varepsilon(\tau)|_{\Delta\phi_1=0^\circ}\right| + \left|\varepsilon(\tau)|_{\Delta\phi_1=180^\circ}\right|}{2} \right] d\tau \tag{29}$$

where $\Delta\phi_1$ is the carrier phase offset between multipath and line of sight (LOS) path, typically 0° or 180°.

Figure 11 shows the multipath error envelope and average multipath error envelope curves of all signals with d = 1 chip, $a = -6$ dB. The multipath error envelopes of Pulse-OTFS(10,1023) and OTFS(10,1023) are significantly lower than that of Pulse-BPSK(5) and BPSK(5) at a geometric path delay of less than 84 m and slightly worse thereafter. For the average multipath error envelope, Pulse-OTFS(10,1023) and OTFS(10,1023) are the best at all geometric path delays. Hence, the proposed signal has better anti-multipath performance than that of the Pulse-BPSK and BPSK signals.

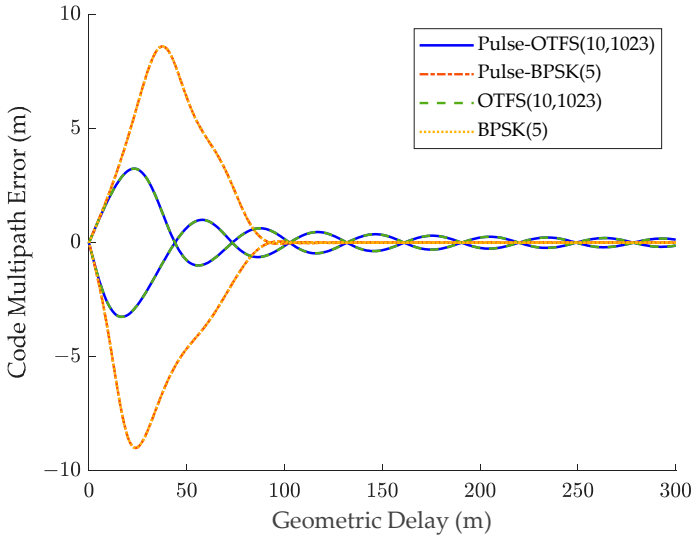

(a)

Figure 11. *Cont.*

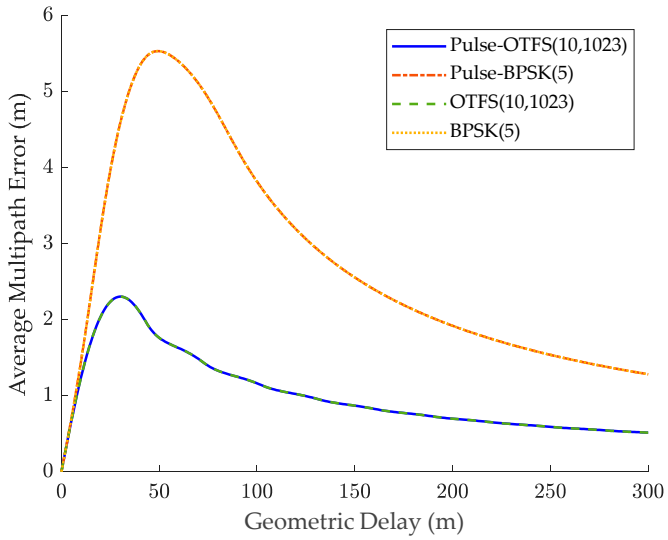

(**b**)

Figure 11. Comparison of anti-multipath performance for different signals. (**a**) Multipath error envelope and (**b**) average multipath error envelope. $a = -6$ dB, $d = 1$ chip.

3.5. Compatibility

The mutual interference and compatibility between different signals are important performance indicators for navigation signals, and the generally used indicator is the spectral separation coefficient (SSC). The SSC measures the amount of interference caused by other signals in the same band. The compatibility of a signal becomes better with decreasing SSC value; its expression is

$$\chi = \int_{-B_r/2}^{B_r/2} G_l(f) G_n(f) \mathrm{d}f \tag{30}$$

where $G_l(f)$ is the normalized PSD of interference signals.

Table 3 shows SSC values for different signals. It can be seen that Pulse-OTFS(10,1023) and OTFS(10,1023) provide the same SSCs and also keep a low level of mutual interference with other signals. The results suggest that Pulse-OTFS has two advantages when utilized as a navigation signal: it minimizes interference with existing GNSS signals and Pulse-OTFS signals from different satellites.

Table 3. SSC values for different signals with a 20 MHz pre-filtering bandwidth.

SSC (dB)	Pulse-OTFS(10,1023)	OTFS(10,1023)	Pulse-BPSK(5)	BPSK(5)
Pulse-OTFS(10,1023)	−70.11	−70.11	−70.32	−70.32
OTFS(10,1023)	−70.11	−70.11	−70.32	−70.32
Pulse-BPSK(5)	−70.32	−70.32	−68.41	−68.41
BPSK(5)	−70.32	−70.32	−68.41	−68.41

The performance of the pulse OTFS signal has been extensively evaluated in this section. In summary, the proposed signal mitigates the high acquisition complexity of the original OTFS and traditional navigation signals to enable fast acquisition of the future massive LEO satellite signals and has good anti-multipath performance with advantages in terms of code-tracking accuracy and compatibility, while the Locata signal also reduces acquisition complexity but its delay measurement precision is not as good as that of the proposed signal.

4. Simulation and Experimental Results

In this section, we design a simulation experiment and implement an experimental platform for transmitting and receiving signals based on SDR to verify the main performance advantages of the proposed signal, mainly including acquisition probability, acquisition complexity, and code-tracking accuracy. We compare the performance of the proposed signal with original OTFS, traditional GNSS, and Locata signals, i.e., OTFS(10,1023), BPSK(5), and Pulse-BPSK(5).

4.1. Simulation

In the previous text, we analyzed the theoretical acquisition performance of the proposed signals. We verify the acquisition probability of the PCS scheme using Monte Carlo simulation for different C/N_0 and Doppler frequency offsets in this section. The simulation experiment process is as follows. We first use a software signal generator to generate a signal stream with a specified Doppler frequency offset. Secondly, a local replica with the closest search frequency to that Doppler is generated. Finally, we perform a large number of PCSs and compare the search results with the threshold to calculate the detection probability. The experimental parameters are set as follows. The signal bandwidth is 10.23 MHz, the sampling rate is 20.46 MHz, the total false alarm probability is 10^{-3}, $N = 10$, $T_{coh} = 1$ ms, and the Doppler frequency offset includes 37.25 kHz, 37.5 kHz, and 40 kHz. Moreover, there are 10^6 Monte Carlo simulations at each C/N_0. The simulated detection probability curves are shown in Figure 12.

The detection probability curves in Figure 12 agree well with the theoretical curves in Figure 8, verifying that the theoretical analysis of detection probability is correct. We can equally reach the following conclusions. The detection probability is the same for two pulsed signals as it is for two continuous signals. All signals have the same and highest acquisition probability at 40 kHz. Meanwhile, the Pulse-OTFS and Pulse-BPSK signals at 37.5 kHz and the OTFS and BPSK signals at 37.25 kHz have the worst acquisition probability. Most importantly, the detection probability of the proposed signal at the same Doppler frequency offset is about 1 dB higher than that of OTFS and BPSK. As a result, the proposed signal is robust to significant Doppler shift scenarios and improves the acquisition probability compared to continuous signals.

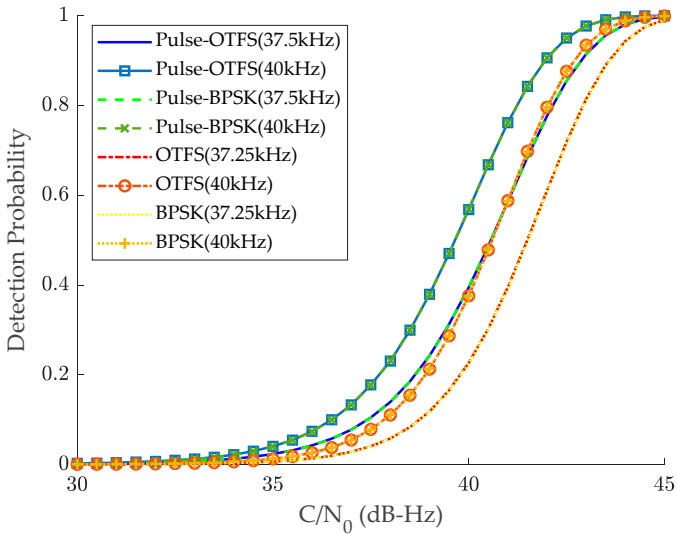

Figure 12. Simulated detection probabilities for different signals.

4.2. Experiment

4.2.1. System Setup

Figure 13 is the operation flowchart of the hardware system. The solid and dashed boxes represent hardware and software components, respectively. As we can see, the

system consists of two universal software radio peripherals (USRPs), a rubidium atomic clock, transmitting and receiving terminals (Tx & Rx computers), an RF attenuator, and a low noise amplifier (LNA). The workflow of the hardware system is as follows. First, the software signal generator generates the discrete-time baseband transmitted signal files and stores them in the Tx computer. The USRP hardware driver (UHD) reads the file and transmits it to the USRP via a network cable; the motherboard and daughterboard in the USRP perform digital-to-analog conversion and up-conversion, respectively. Another USRP receives the RF signals which pass through the RF attenuator and the LNA. The UHD in the Rx computer saves the down-converted and analog-to-digital converted signals as discrete-time signal files via a network cable. Finally, the software receiver post-processes the saved signal file. The RF attenuator can be adjusted to obtain the desired C/N_0. The rubidium atomic clock provides a high-precision frequency reference for the two USRPs to eliminate the frequency offset between the received and transmitted signals. A photograph of the hardware system based on SDR is shown in Figure 14.

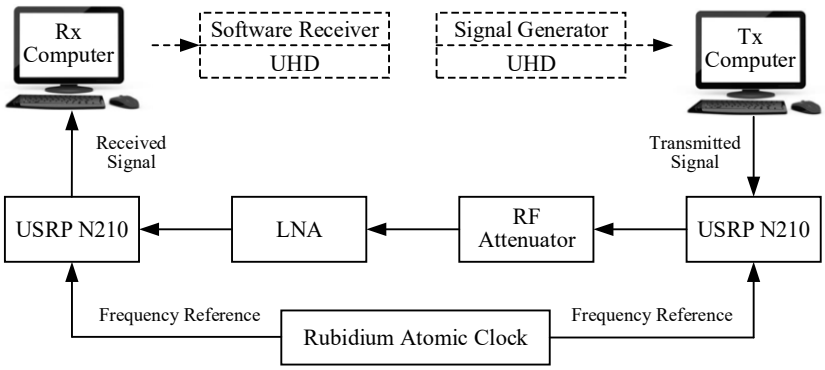

Figure 13. Flow chart of the experimental platform.

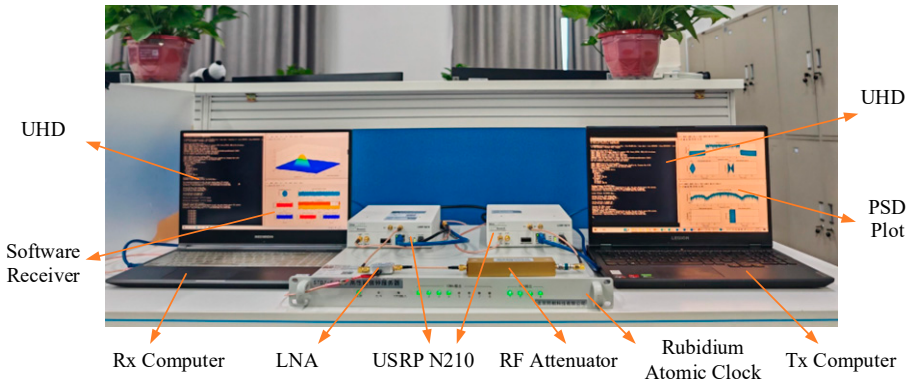

Figure 14. Photograph of the experimental platform.

The carrier frequency of the RF frequency is 2 GHz. The master clock rate of USRP N210 is 100 MHz, and the sampling rate supported is limited to dividing the master clock rate by an integer factor. Therefore, the sampling rate is set to 20 MHz, the delay bins $M = 1023$, and the Doppler bins $N = 10$; thus, the duty cycle of the Pulse-OTFS and Pulse-BPSK is set to 0.1.

We have developed software receivers for Pulse-OTFS(10,1023), OTFS(10,1023), Pulse-BPSK(5), and BPSK(5). They use the same tracking loop as the traditional navigation receivers. The difference is only in the local replica generation. Due to the short period of the pulsed signals, the closed-loop estimator is still able to track the signals stably. The C/N_0 setting for the received signal is 25 dB·Hz to 45 dB·Hz (10 ms coherent integration time) and 35 dB·Hz to 55 dB·Hz (1 ms coherent integration time). The interval is 5 dB·Hz.

The equivalent noise bandwidth of DLL is 1 Hz, the early–late spacing of the correlator is 1 chip, and the phase lock loop (PLL) bandwidth is 10 Hz.

The experimental parameters are listed in Table 4. The first five items are signal parameters, the last four items are software receiver configuration parameters.

Table 4. Experiment parameters.

Parameter	Value
RF frequency	2 GHz
Sampling rate	20 MHz
Signal bandwidth (B)	10.23 MHz
Signal period (NT)	1 ms
Duty cycle ($1/N$)	0.1
Coherent integration time (T_{coh})	1 ms or 10 ms
Early–late spacing of the correlator	1 chip
Bandwidth of the DLL	1 Hz
Bandwidth of the PLL	10 Hz

4.2.2. Experimental Results and Discussion

The signal files stored in the Rx computer were post-processed using the software receiver for statistics code-tracking accuracy. For all compared signals, the mean value of the tracking accuracy for each C/N_0 was calculated for five groups of signal files, each with 2000 ms (DLL steady state output). Figure 15a,b show the experimental code-tracking accuracy for the DLL with coherent integration times of 1 ms and 10 ms, respectively.

The lowest C/N_0 in Figure 15a,b is 35 dB·Hz and 25 dB·Hz, respectively. Because the coherent integration time determines the tracking threshold of the loop. From Figure 15b, we can see that the proposed signal is still able to track the signal stably even at a shallow C/N_0 level. This indicates that the proposed signal is robust in high-noise scenarios. Figure 15 illustrates that the code-tracking accuracy of pulsed and continuous signals with the same modulation is approximately the same. The C/N_0 of Pulse-OTFS(10,1023) and OTFS(10,1023) is about 8 dB lower compared to Pulse-BPSK(5) and BPSK(5) with the same code-tracking accuracy; in other words, the proposed signal has a higher delay measurement accuracy with the same C/N_0. Because Pulse-OTFS(10,1023) has a steeper main peak of the autocorrelation function with the same bandwidth, as shown in Figure 4, this benefits delay resolution and measurement accuracy. At medium and high C/N_0, the experimental results agree well with the theoretical results in Figure 9b, although the experimental results have a minor deviation from the latter.

Figure 16 gives a plot of the magnitude of the correlator peaks corresponding to the correct code phase in the signal acquisition process. It reflects the variation in the correlation loss at different Doppler frequency offsets. The C/N_0 is 55 dB·Hz for all received signals, and the Doppler frequency search interval is 500 Hz. From the figure, we can see that the correlation loss of the pulsed signals is much lower than that of the continuous signals. Table 5 lists the magnitude values of correlator peaks corresponding to different Doppler frequency offsets in Figure 16. Specifically, the correlation peak magnitudes for all signals are approximately the same at 0 Hz, and the acquisition results have no loss. The correlation peak magnitudes of Pulse-OTFS(10,1023) and Pulse-BPSK(5) at $\pm$0.5 kHz decrease little, but they suffer severe loss for OTFS(10,1023) and BPSK(5). It is not until the Doppler frequency offset of $\pm$5 kHz that the correlation peak magnitudes of Pulse-OTFS(10,1023) and Pulse-BPSK(5) reach the level of OTFS(10,1023) and BPSK(5) at $\pm$0.5 kHz. The tolerable frequency offset of the pulsed signal is 10 times that of a continuous signal, and the proposed signal can therefore be searched with a Doppler search interval 10 times that of BPSK(5). This enables the proposed signal to search for the Doppler frequency using large steps, thus speeding up the signal acquisition process.

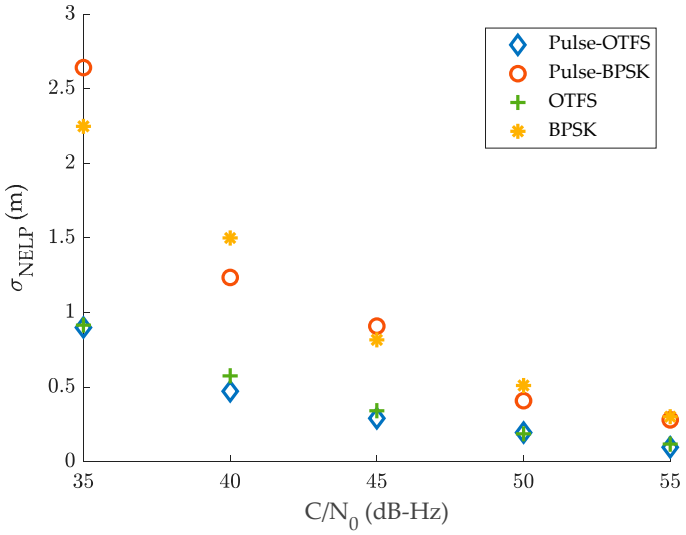

(**a**)

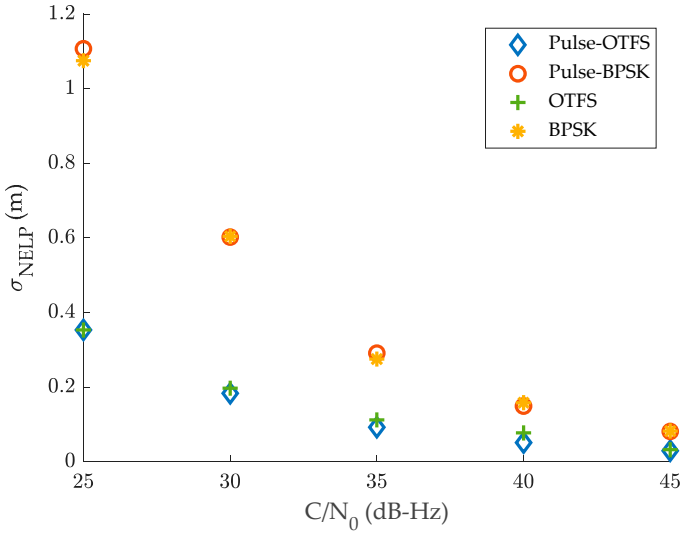

(**b**)

Figure 15. Experimental results of the NELP DLL code-tracking error. (**a**) T_{coh} = 1 ms and (**b**) T_{coh} = 10 ms.

Table 5. Magnitude values of correlator peaks for different signals.

Doppler Frequency Offset (kHz)	Pulse-OTFS(10,1023)	Pulse-BPSK(5)	OTFS(10,1023)	BPSK(5)
0	21.30	21.94	21.30	20.98
+0.5	21.14	21.71	14.39	13.48
−0.5	21.28	21.92	12.99	13.56
+5	12.39	12.88	1.27	1.79
−5	13.46	14.41	0.83	0.57

To verify the acquisition efficiency of the proposed signal in the hardware system, we counted the average running time of 100 times the acquisition program with the PCS scheme in different Doppler frequencies, as shown in Table 6. We can see that the running time of the program is close to the same at 0 Hz and 40 kHz Doppler frequency offset. This is because we use a commonly employed detection and decision method, which searches for all correlation results in Doppler frequency points and finds the maximum value before

making a decision. Therefore, the running time is practically independent of the Doppler frequency offset. We calculate that the running time of the acquisition program decreased by about 89.3% and 88.5% for Pulse-OTFS and Pulse-BPSK, respectively. This result is in agreement with the 89.4% reduction in theoretical acquisition complexity in Section 3.2.2.

Table 6. Average running time of acquisition programs for different signals (s).

Doppler Frequency Offset (kHz)	Pulse-OTFS(10,1023)	Pulse-BPSK(5)	OTFS(10,1023)	BPSK(5)
0 Hz	0.015	0.017	0.142	0.144
40 kHz	0.016	0.016	0.144	0.147

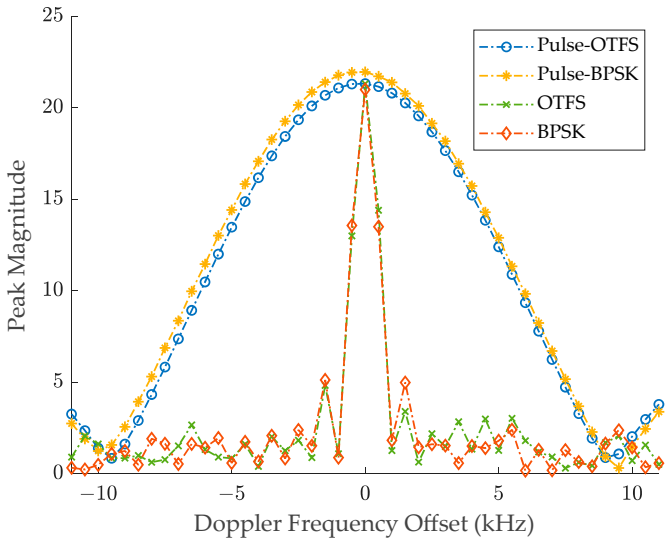

Figure 16. Correlator peak magnitude for different signals.

The above experiments verified that the proposed signal has both the high accuracy measurement of the OTFS signal and the low acquisition complexity of the pulsed signal. Furthermore, the proposed navigation signal occupies at most 10% of the signal period in the time domain, the transmission of communication signals for the rest of the time does not cause interference between the signals, and since the OTFS modulation itself is designed for broadband communication, the navigation and communication signals can share a common modulator, thus simplifying the design of the satellite payload. It can be concluded that the proposed signal would be an advantageous choice for use as a future broadband LEO satellite navigation signal.

5. Conclusions

This work proposes a novel signal called Pulse-OTFS. We have derived analytical ACF and PSD expressions for OTFS modulation, which are also applicable to the proposed signal. The results of the navigation performance evaluation show that the acquisition complexity decreases with the increase in the Doppler number N. The acquisition complexity of Pulse-OTFS is at least 89.4% lower than that of the continuous GNSS signals where N is not less than 10, which effectively reduces the acquisition time of LEO signals, and at the same time, the acquisition probability of the proposed signal is about 1 dB higher than that of the latter with a total false alarm probability of 10^{-3}. In terms of measurement precision, Pulse-OTFS has a steep ACF main peak and a large Gabor bandwidth; its delay measurement accuracy is about 8 dB higher than that of BPSK and Pulse-BPSK signals. The analysis of the S-curve demonstrates that the proposed signal is capable of unambiguous tracking. Moreover, Pulse-OTFS has a smaller SSC value and lower multipath error envelope than that of BPSK and Pulse-BPSK signals, which suggests that it has good compatibility with

other navigation signals in the same frequency band and better theoretical anti-multipath performance. The experimental results validate the advantages of fast acquisition and high-precision measurements of the proposed signal. Pulse-OTFS is easy to integrate with communication signals and can be used as a navigation signal from broadband LEO satellites as an effective complement to the GNSS.

Author Contributions: Conceptualization, D.F., H.L. and G.O.; methodology, D.F. and M.Y.; software, D.F. and M.Y.; validation, M.M. and G.O.; formal analysis, D.F. and H.L.; investigation, D.F.; resources, H.L.; data curation, D.F.; writing—original draft preparation, D.F.; writing—review and editing, H.L. and M.M.; visualization, D.F. All authors have read and agreed to the published version of the manuscript.

Funding: This research was funded by the National Key Research and Development Program of China, grant number 2023YFC2205400, and the National Natural Science Foundation of China, grant number U20A0193.

Data Availability Statement: The raw data supporting the conclusions of this article will be made available by the authors on request.

Conflicts of Interest: The authors declare no conflicts of interest. The funders had no role in the design of the study; in the collection, analysis, or interpretation of the data; in the writing of the manuscript; or in the decision to publish the results.

References

1. Kassas, Z.M. Navigation from Low-Earth Orbit: Part 2: Models, Implementation, and Performance. In *Position, Navigation, and Timing Technologies in the 21st Century*; Morton, Y.J., van Diggelen, F., Spilker, J.J., Jr., Parkinson, B.W., Eds.; Wiley: Hoboken, NJ, USA, 2020; pp. 1381–1412.
2. Reid, T.G.R.; Neish, A.M.; Walter, T.; Enge, P.K. Broadband LEO Constellations for Navigation: Broadband LEOs for Navigation. *J. Inst. Navig.* **2018**, *65*, 205–220. [CrossRef]
3. Reid, T.; Gunning, K.; Perkins, A.; Lo, S.; Walter, T. Going Back for the Future: Large/Mega LEO Constellations for Navigation. In Proceedings of the 32nd International Technical Meeting of the Satellite Division of The Institute of Navigation (ION GNSS+ 2019), Miami, FL, USA, 16–20 September 2019; pp. 2452–2468.
4. Joerger, M.; Gratton, L.; Pervan, B.; Cohen, C.E. Analysis of Iridium-Augmented GPS for Floating Carrier Phase Positioning. *Navig. J. Inst. Navig.* **2010**, *57*, 137–160. [CrossRef]
5. Kassas, Z.M.; Khairallah, N.; Kozhaya, S. Ad Astra: Simultaneous Tracking and Navigation with Megaconstellation LEO Satellites. *IEEE Aerosp. Electron. Syst.* **2024**, *39*, 3267440. [CrossRef]
6. Yao, Z.; Lu, M. *Next-Generation GNSS Signal Design: Theories*; Principles and Technologies; Springer: Singapore, 2021; pp. 15–38.
7. Hegarty, C.; Kaplan, E. *Understanding GPS: Principles and Applications*, 2nd ed.; Artech House: Norwood, MA, USA, 2005; pp. 83–88.
8. Betz, J.W. Binary Offset Carrier Modulations for Radionavigation. *Navigation* **2001**, *48*, 227–246. [CrossRef]
9. Hein, G.W.; Avila-Rodriguez, J.-A.; Wallner, S.; Pratt, A.R.; Owen, J.; Issler, J.-L.; Betz, J.W.; Hegarty, C.J.; Lenahan, S.; Rushanan, J.J. MBOC: The New Optimized Spreading Modulation Recommended for GALILEO L1 OS and GPS L1C. In Proceedings of the 2006 IEEE/ION Position, Location, And Navigation Symposium, San Diego, CA, USA, 25 April 2006; pp. 883–892.
10. Lestarquit, L.; Artaud, G.; Issler, J. AltBOC for Dummies or Everything You Always Wanted to Know About AltBOC. In Proceedings of the 21st International Technical Meeting of the Satellite Division of the Institute of Navigation (ION GNSS 2008), Savannah, GA, USA, 16–19 September 2008; pp. 961–970.
11. Kowatsch, M.; Lafferl, J. A Spread-Spectrum Concept Combining Chirp Modulation and Pseudonoise Coding. *IEEE Trans. Commun.* **1983**, *31*, 1133–1142. [CrossRef]
12. Zhao, X.; Huang, X.; Tang, X.; Feng, X.; Sun, G. Chirp Pseudo-Noise Signal and Its Receiving Scheme for LEO Enhanced GNSS. *IET Radar Sonar Navig.* **2022**, *16*, 34–50. [CrossRef]
13. Xiao, L.; Li, S.; Qian, Y.; Chen, D.; Jiang, T. An Overview of OTFS for Internet of Things: Concepts, Benefits, and Challenges. *IEEE Internet Things J.* **2022**, *9*, 7596–7618. [CrossRef]
14. Xiao, L.; Liu, G.; Xiao, P.; Jiang, T. Error Probability Analysis for Rectangular Differential OFDM With Index Modulation Over Dispersive Channels. *IEEE Wirel. Commun. Lett.* **2021**, *10*, 2795–2799. [CrossRef]
15. Xue, L.; Li, X.; Wu, W.; Dong, J. Multifunctional Signal Design for Measurement, Navigation and Communication Based on BOC and BPSK Modulation. *Remote Sens.* **2022**, *14*, 1653. [CrossRef]

16. Deng, L.; Yang, Y.; Ma, J.; Feng, Y.; Ye, L.; Li, H. OFDM-BOC: A Broadband Multicarrier Navigation Modulation-Based BOC for Future GNSS. *IEEE Trans. Veh. Technol.* **2023**, *73*, 3964–3979. [CrossRef]
17. Wang, D.; Michel, F. OFDM Transmission for Time-Based Range Estimation. *IEEE Signal Process. Lett.* **2010**, *17*, 571–574. [CrossRef]
18. Liu, X.; Liang, M.; Morton, Y.; Closas, P.; Zhang, T.; Hong, Z. Performance Evaluation of MSK and OFDM Modulations for Future GNSS Signals. *GPS Solut.* **2014**, *18*, 163–175. [CrossRef]
19. del Peral-Rosado, J.A.; L'opez-Salcedo, J.A.; Seco-Granados, G.; Zanier, F.; Crisci, M. Analysis of Positioning Capabilities of 3GPP LTE. In Proceedings of the 25th International Technical Meeting of the Satellite Division of The Institute of Navigation (ION GNSS 2012), Nashville, TN, USA, 17–21 September 2012; pp. 650–659.
20. Shamaei, K.; Khalife, J.; Kassas, Z.M. Exploiting LTE Signals for Navigation: Theory to Implementation. *IEEE Trans. Wirel. Commun.* **2018**, *17*, 2173–2189. [CrossRef]
21. Fischer, S. 5G NR Positioning. In *5G and Beyond*; Lin, X., Lee, N., Eds.; Springer International Publishing: Cham, Switzerland, 2021; pp. 429–483.
22. Shamaei, K.; Kassas, Z.M. Receiver Design and Time of Arrival Estimation for Opportunistic Localization with 5G Signals. *IEEE Trans. Wirel. Commun.* **2021**, *20*, 4716–4731. [CrossRef]
23. Hadani, R.; Rakib, S.; Tsatsanis, M.; Monk, A.; Goldsmith, A.J.; Molisch, A.F.; Calderbank, R. Orthogonal Time Frequency Space Modulation. In Proceedings of the 2017 IEEE Wireless Communications and Networking Conference (WCNC), San Francisco, CA, USA, 19–22 March 2017; pp. 1–6.
24. Das, S.S.; Prasad, R. *Orthogonal Time Frequency Space Modulation: OTFS a Waveform for 6G*, 1st ed.; River Publishers: New York, NY, USA, 2022; pp. 5–8.
25. Hong, Y.; Thaj, T.; Viterbo, E. *Delay-Doppler Communications: Principles and Applications*; Academic Press: London, UK; San Diego, CA, USA; Cambridge, MA, USA; Oxford, UK, 2023; pp. 202–210.
26. Liao, Y.; Liu, S.; Hong, X.; Shi, J.; Cheng, L. Integration of Communication and Navigation Technologies toward LEO-Enabled 6G Networks: A Survey. *Space Sci. Technol.* **2023**, *3*, 0092. [CrossRef]
27. Foreman-Campins, G.; López-Salcedo, J.A.; Lohan, E.S. Orthogonal Time Frequency Space Modulation (OTFS) for Positioning Using LEO Satellites. In Proceedings of the 2024 36th Conference of Open Innovations Association (FRUCT), Lappeenranta, Finland, 30 October–1 November 2024; pp. 1–4.
28. Wang, S.; Tang, X.; Lei, J.; Ma, C.; Wen, C.; Sun, G. High-Precision Doppler Frequency Estimation Based Positioning Using OTFS Modulations by Red and Blue Frequency Shift Discriminator. *China Commun.* **2024**, *21*, 17–31. [CrossRef]
29. Li, Y.; Zhang, G.; Yu, J.; Li, G.; Li, Y. OTFS-Based Communication and Navigation Integrated Signal Transmission for LEO Satellites. In Proceedings of the 2022 IEEE 22nd International Conference on Communication Technology (ICCT), Nanjing, China, 11 November 2022; IEEE: New York, NY, USA, 2023; pp. 451–457.
30. Ma, T.; Xu, Y.; Ou, X.; Huang, Y.; He, D.; Zhang, W. Iterative Channel Estimation for OTFS Using ZC Sequence with Low Peak-to-Average Power Ratio. In Proceedings of the ICC 2023—IEEE International Conference on Communications, Rome, Italy, 28 May–1 June 2023; IEEE: New York, NY, USA, 2023; pp. 2276–2281.
31. Li, S.; Zhang, M.; Ju, C.; Wang, D.; Chen, W.; Zhou, P.; Wang, D. Downlink Carrier Frequency Offset Estimation for OTFS-Based LEO Satellite Communication System. *IEEE Commun. Lett.* **2024**, *28*, 163–167. [CrossRef]
32. Gong, Z.; Jiang, F.; Li, C.; Shen, X. Simultaneous Localization and Communications with Massive MIMO-OTFS. *IEEE J. Select. Areas Commun.* **2023**, *41*, 3908–3924. [CrossRef]
33. Barnes, J.; Rizos, C.; Kanli, M.; Pahwa, A.; Small, D.; Voigt, G.; Gambale, N.; Lamance, J. High Accuracy Positioning Using Locata's next Generation Technology. In Proceedings of the 18th International Technical Meeting of the Satellite Division of The Institute of Navigation (ION GNSS 2005), Long Beach, CA, USA, 13–16 September 2005; pp. 2049–2056.
34. Rizos, C.; Yang, L. Background and Recent Advances in the Locata Terrestrial Positioning and Timing Technology. *Sensors* **2019**, *19*, 1821. [CrossRef]
35. Rizos, C. Locata: A Positioning System for Indoor and Outdoor Applications Where GNSS Does Not Work. In Proceedings of the 18th Association of Public Authority Surveyors Conference (APAS2013), Canberra, Australia, 12–14 March 2013; pp. 73–83.
36. Talbot, S.L.; Farhang-Boroujeny, B. Spectral Method of Blind Carrier Tracking for OFDM. *IEEE Trans. Signal Process.* **2008**, *56*, 2706–2717. [CrossRef]
37. Liu, C.; Li, F. On Spectrum Modeling of OFDM Signals for Digital Broadcasting. In Proceedings of the Proceedings 7th International Conference on Signal Processing, 2004. Proceedings. ICSP '04. 2004, Beijing, China, 31 August–4 September 2004; IEEE: New York, NY, USA, 2004; pp. 1886–1889.
38. 3GPP. *Study on New Radio (NR) to Support Non-Terrestrial Networks*; 3rd Generation Partnership Project (3GPP): Valbonne, France, 2020; pp. 88–95.
39. Betz, J.W.; Kolodziejski, K.R. Generalized Theory of Code Tracking with an Early-Late Discriminator Part I: Lower Bound and Coherent Processing. *IEEE Trans. Aerosp. Electron. Syst.* **2009**, *45*, 1538–1556. [CrossRef]
40. Betz, J.W.; Kolodziejski, K.R. Generalized Theory of Code Tracking with an Early-Late Discriminator Part II: Noncoherent Processing and Numerical Results. *IEEE Trans. Aerosp. Electron. Syst.* **2009**, *45*, 1557–1564. [CrossRef]

41. Van Nee, R.D.J. Spread-Spectrum Code and Carrier Synchronization Errors Caused by Multipath and Interference. *IEEE Trans. Aerosp. Electron. Syst.* **1993**, *29*, 1359–1365. [CrossRef]
42. Irsigler, M.; Avila-Rodriguez, J.A.; Hein, G.W. Criteria for GNSS Multipath Performance Assessment. In Proceedings of the 18th International Technical Meeting of the Satellite Division of The Institute of Navigation (ION GNSS 2005), Long Beach, CA, USA, 13–16 September 2005; pp. 2166–2177.